Supporting Information

Enhanced pH-universal hydrogen evolution reactions on the Ru/*a*-Ni-MoO_3 electrocatalysts

Lingyi Peng,[a] Ding Zhang,[a] Zhipeng Ma,[a] Dewei Chu,[b] Claudio Cazorla,[c] Rose Amal,[a] Zhaojun Han,[a, d, *]

a School of Chemical Engineering, The University of New South Wales, Sydney, NSW 2052, Australia

b School of Materials Science and Engineering, The University of New South Wales, Sydney, NSW 2052, Australia

c Department of Physics, Polytechnic University of Catalonia (UPC), C/ Jordi Girona 1-3, Campus Nord, B4-203 08034 Barcelona, Spain

d CSIRO Manufacturing, 36 Bradfield Road, Lindfield, NSW 2070, Australia

Corresponding authors email:

zhaojun.han@unsw.edu.au (Z. Han)

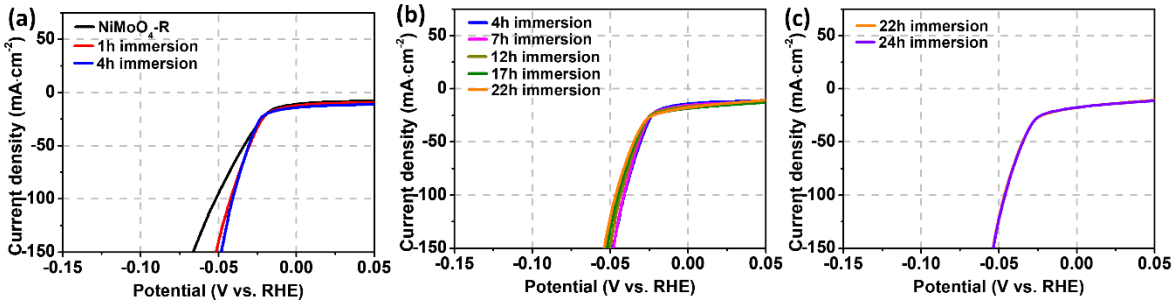

Figure S1. Polarization curves in 1 M KOH after immersion of $NiMoO_4$-R in 1 mg/ml $RuCl_3$ solution for (a) 0–4 h, (b) 4–22 h and (c) 22-24 h. The activity increased within the first 4 h due to the Ru deposition, slightly decreased afterwards likely owing to the dissolution of residual unstable Ni species and stabilized after 22 h.

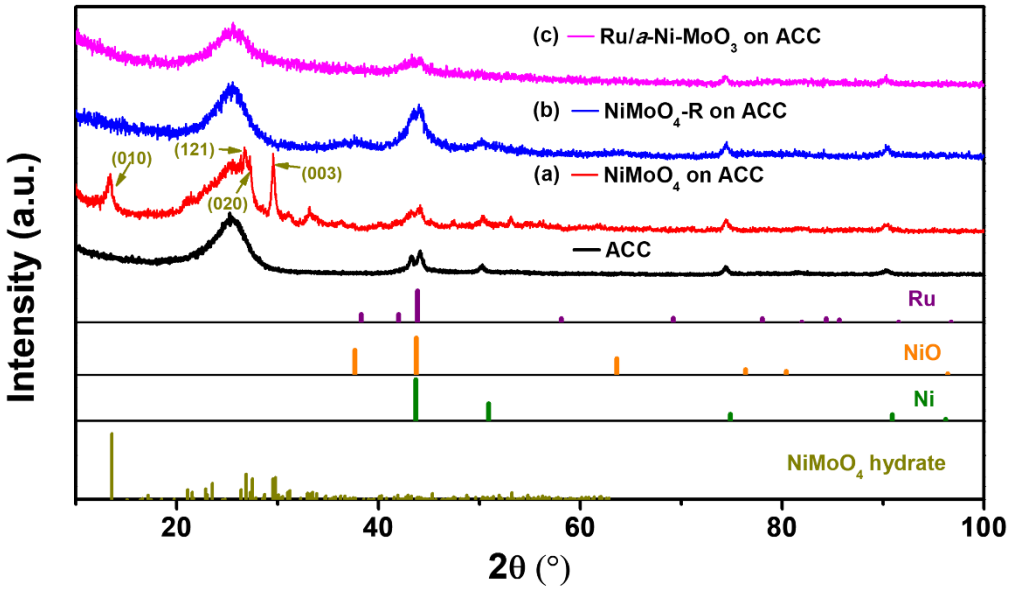

Figure S2. XRD patterns of ACC, (a) $NiMoO_4$ on ACC, (b) $NiMoO_4$-R on ACC, and (c) Ru/*a*-Ni-MoO_3 on ACC. It should be noted that the Ru peaks in Ru/*a*-Ni-MoO_3 were overlapped with the peaks of ACC.

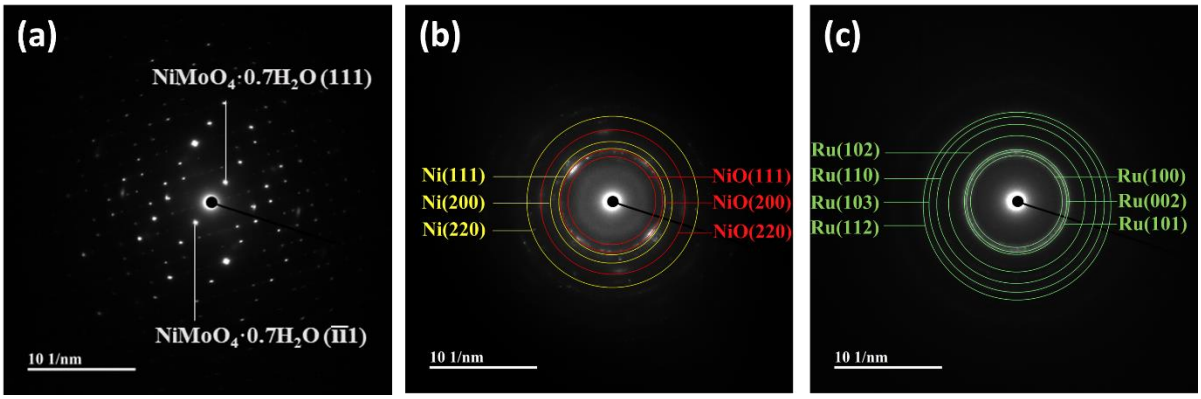

Figure S3. Selected-area electron diffraction patterns of (a) $NiMoO_4$, (b) $NiMoO_4$-R, and (c) Ru/*a*-Ni-MoO_3.

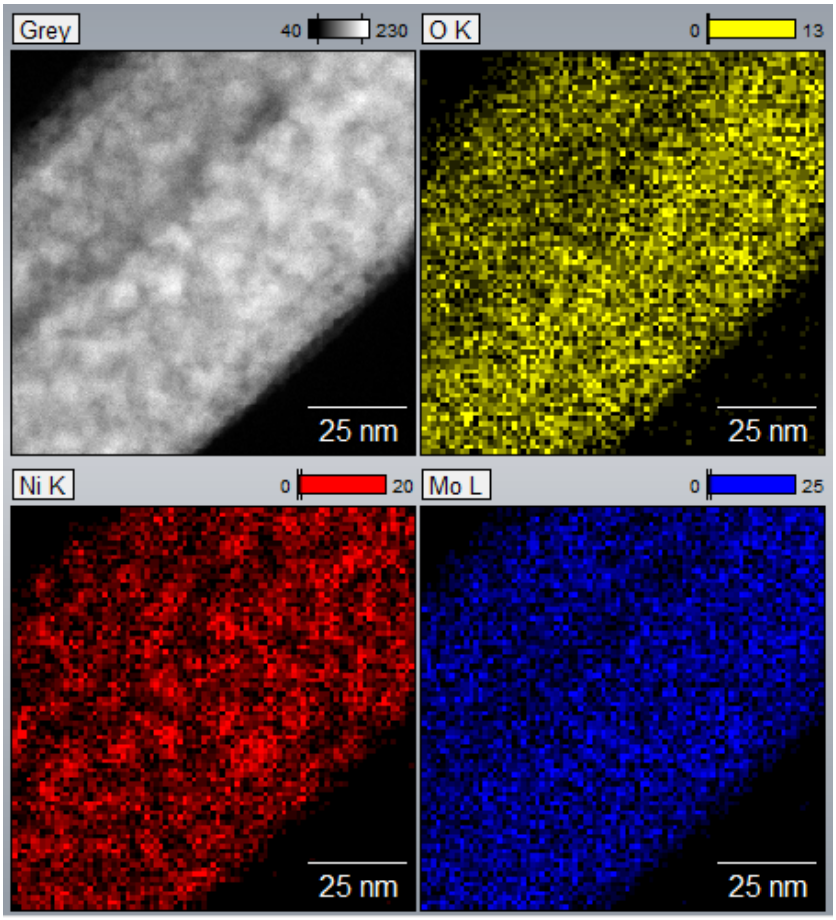

Figure S4. Scanning transmission electron microscopy-energy dispersive X-ray spectroscopy images of $NiMoO_4$-R.

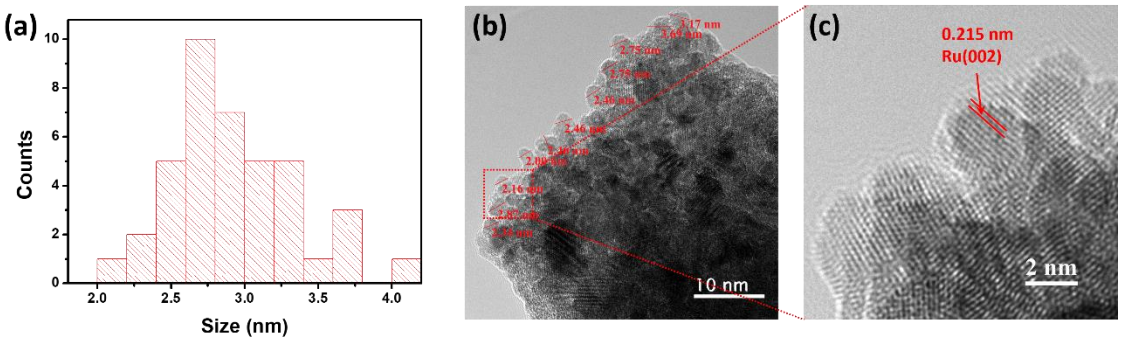

Figure S5. (a) Size distribution histogram of Ru nanoparticles in Ru/*a*-Ni-MoO_3; (b) typical TEM image of Ru/*a*-Ni-MoO_3 showing the measured sizes of Ru nanoparticles; (c) high magnification TEM image showing the lattice spacing assigned to Ru.

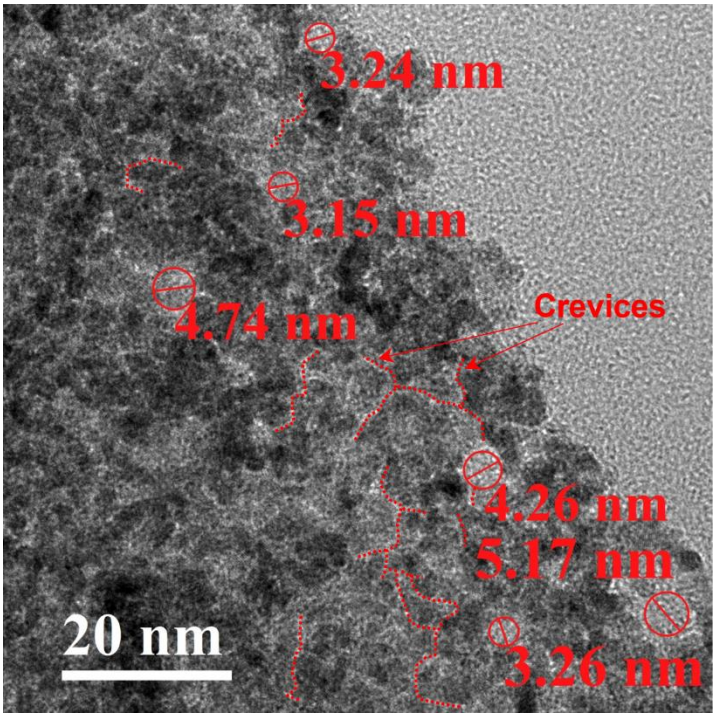

Figure S6. Typical TEM image of Ru/*a*-Ni-MoO_3 showing the crevices and possible mesopores among the Ru nanoparticles.

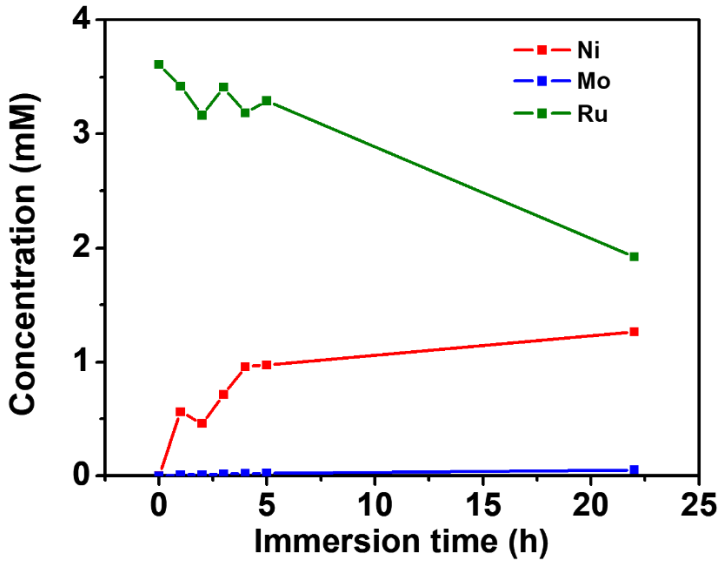

Figure S7. The evolutions of Ni, Ru, and Mo concentrations in the immersion solution obtained by ICP-OES. The rapid change in Ni and Ru concentrations within the first 4 h was due to the redox reaction between Ru^{3+} and the metallic Ni in $NiMoO_4$-R; beyond 4 h the slight increase in Ni concentration was due to dissolution of unstable Ni species, while the decrease in Ru concentration was caused by hydrolysis.

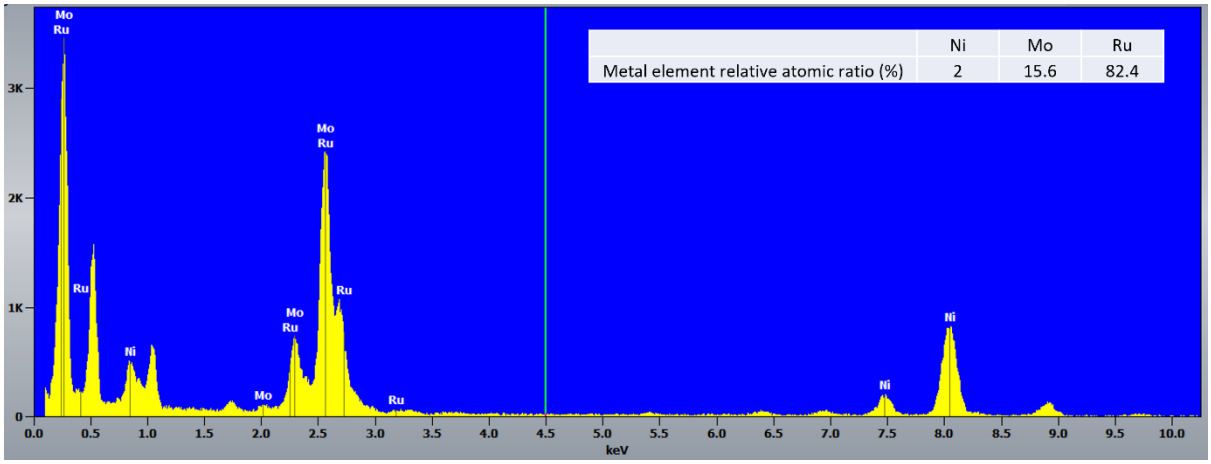

Figure S8. STEM-EDS spectrum and quantitative elemental analysis of Ru/a-Ni-MoO_3.

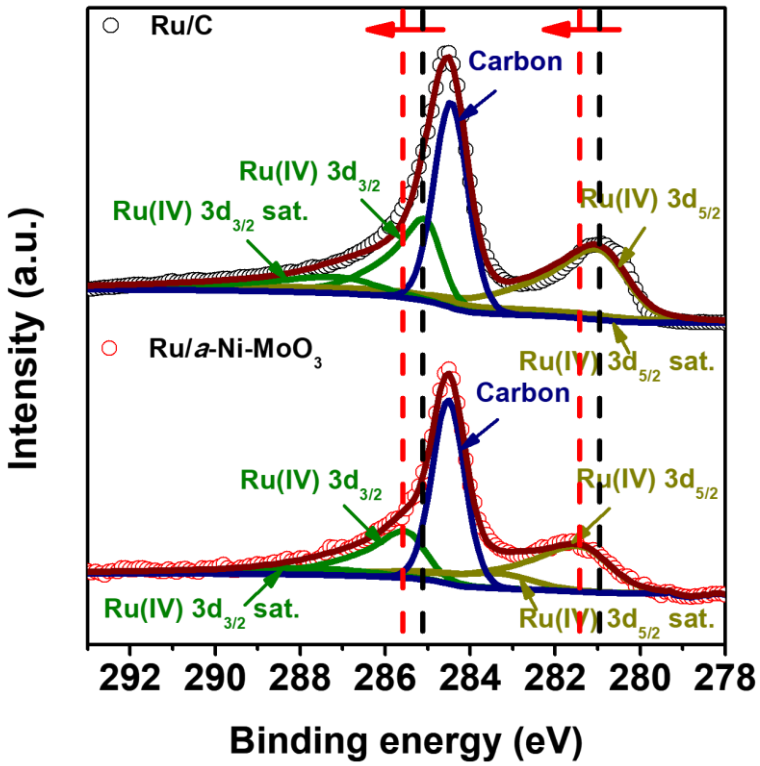

Figure S9. High-resolution XPS Ru 3d spectra of Ru/C and Ru/a-Ni-MoO_3.

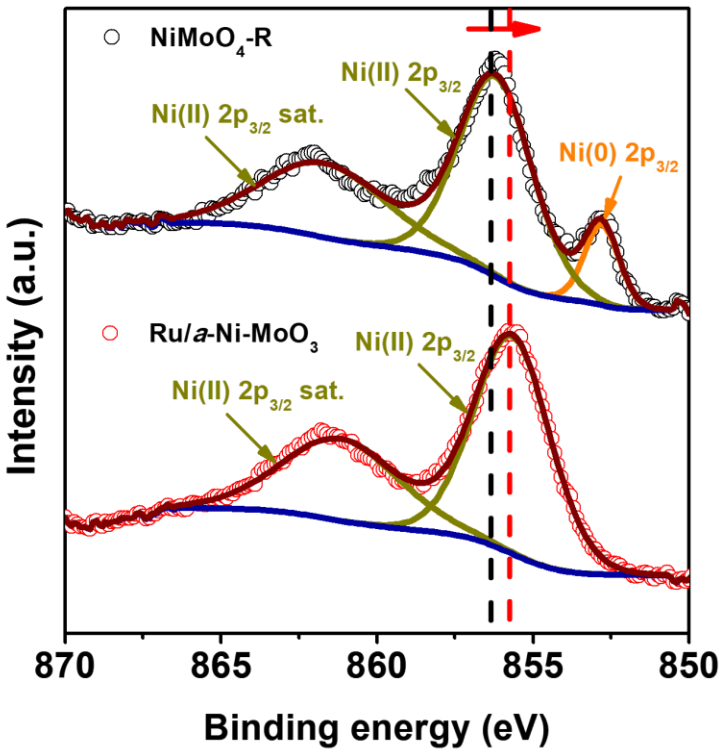

Figure S10. High-resolution XPS Ni $2p_{3/2}$ spectra of $NiMoO_4$-R and Ru/a-Ni-MoO_3.

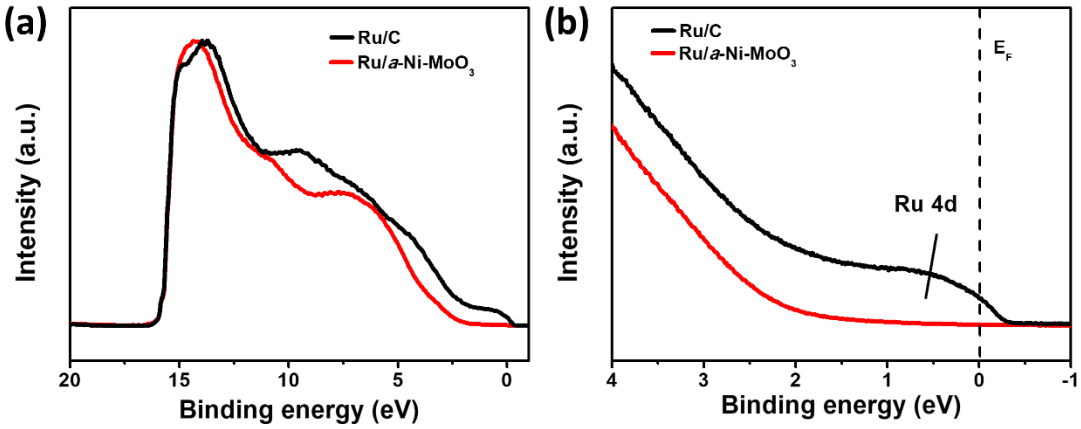

Figure S11. Ultraviolet photoelectron spectroscopy (UPS) (a) survey and (b) Fermi edge spectra of Ru/C and Ru/a-Ni-MoO_3.

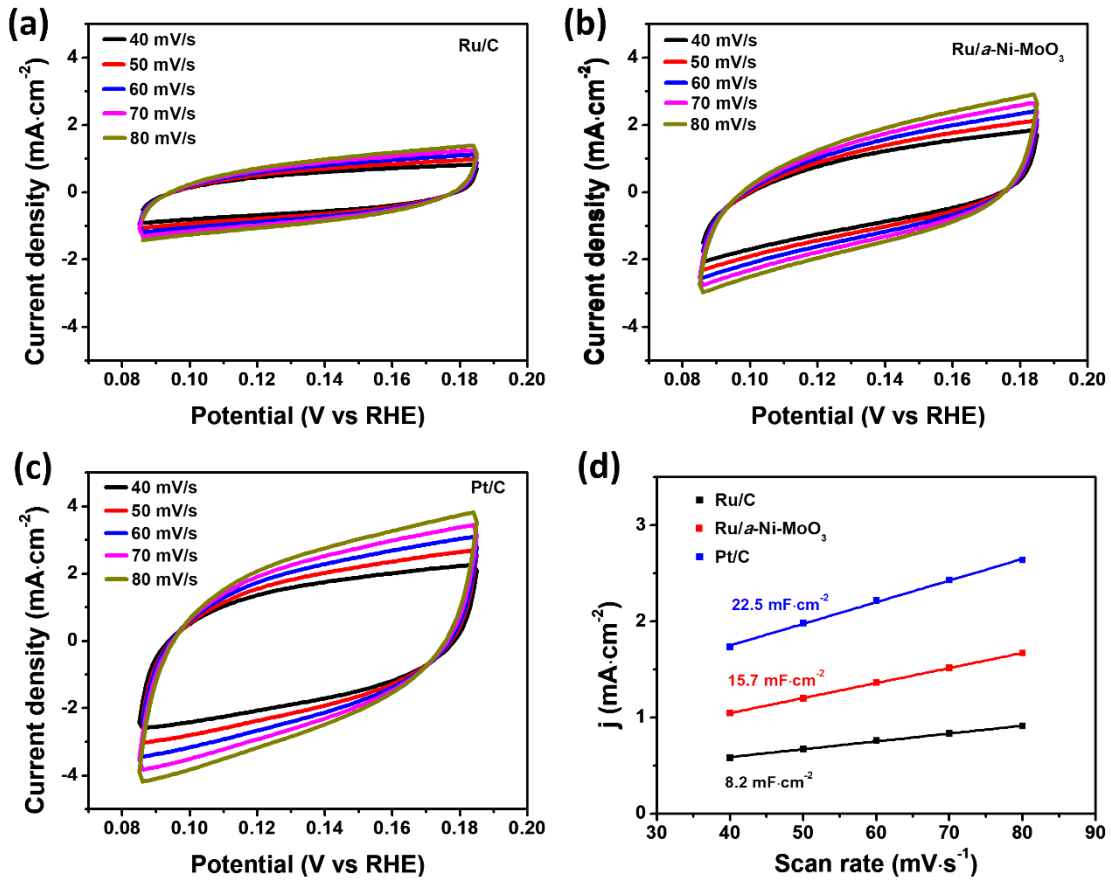

Figure S12. Cyclic voltammetry (CV) curves of (a) Ru/C, (b) Ru/*a*-Ni-MoO_3, and (c) Pt/C in the non-Faradaic regions in 0.5 M H_2SO_4; (d) plots of Δj/2 (the mean value of absolute current density value at the middle point of positive and negative scans in the CV curves) versus scan rate.

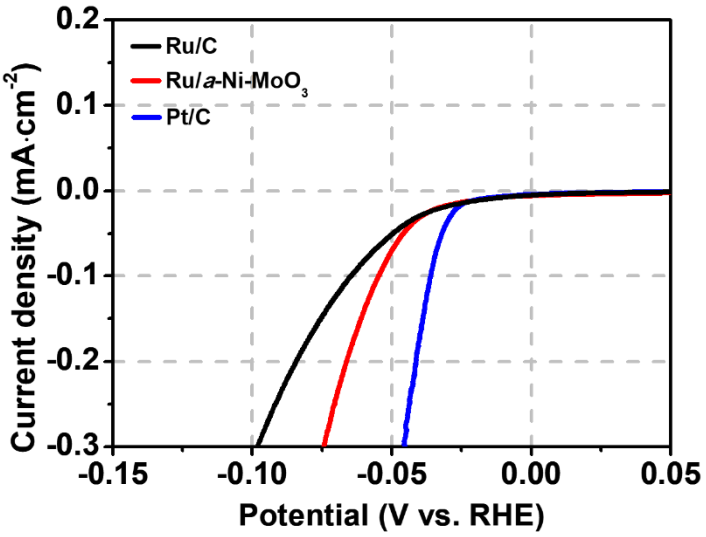

Figure S13. Electrochemical surface area (ECSA) normalized polarization curves of Ru/C, Ru/*a*-Ni-MoO_3, and Pt/C in 0.5 M H_2SO_4; scan rate: 5 mV/s.

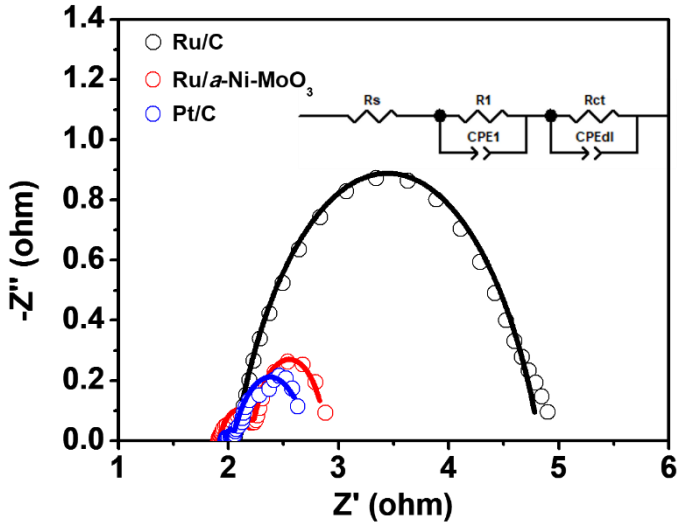

Figure S14. EIS spectra of Ru/C, Ru/*a*-Ni-MoO_3, and Pt/C under an overpotential of -71 mV in 0.5 M H_2SO_4. Inset shows the equivalent circuit model.

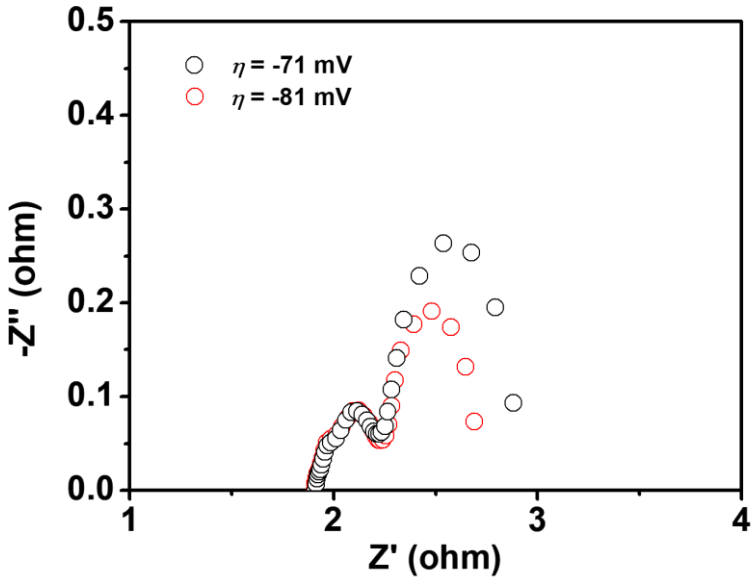

Figure S15. EIS spectra of Ru/*a*-Ni-MoO_3 under different overpotentials in 0.5 M H_2SO_4.

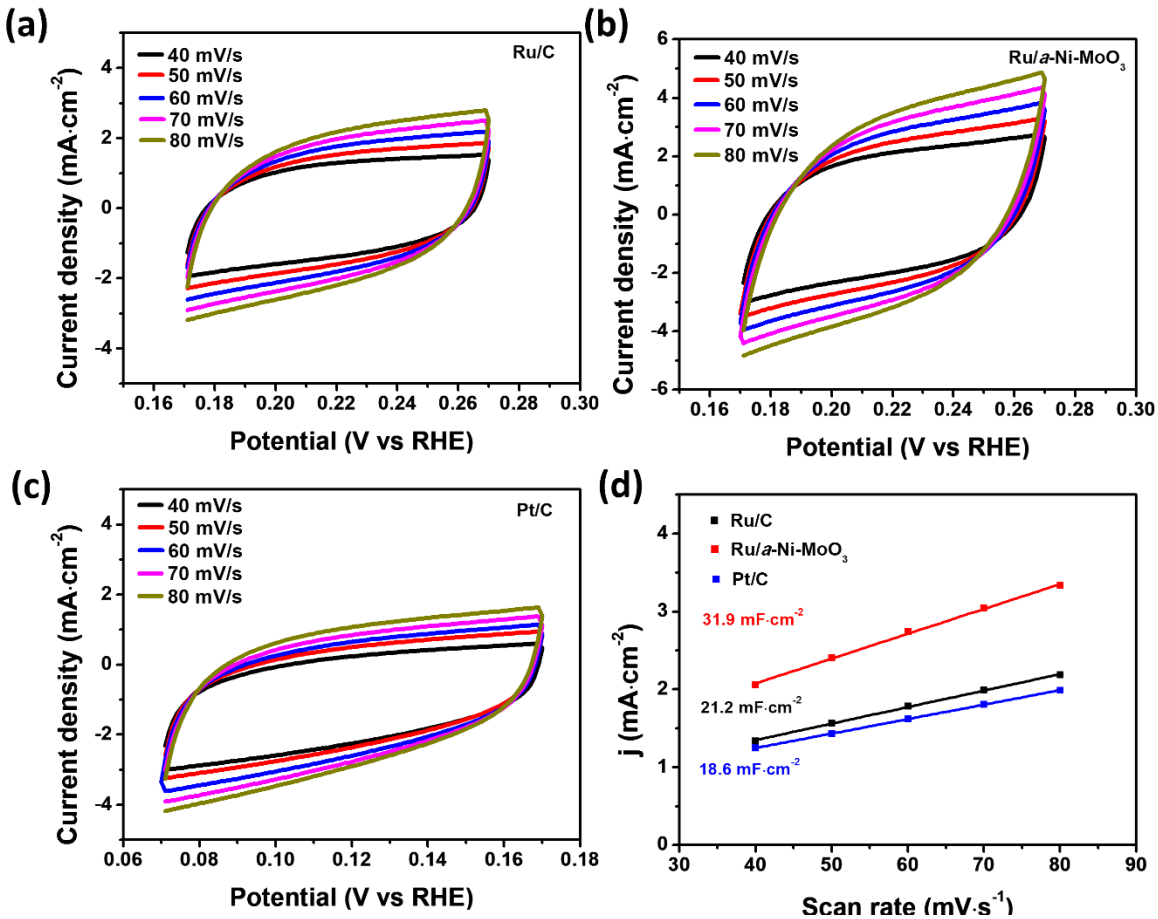

Figure S16. CV curves of (a) Ru/C, (b) Ru/*a*-Ni-MoO_3, and (c) Pt/C in the non-Faradaic regions in 1 M KOH; (d) plots of Δj/2 (the mean value of absolute current density value at the middle point of positive and negative scans in the CV curve) versus scan rate.

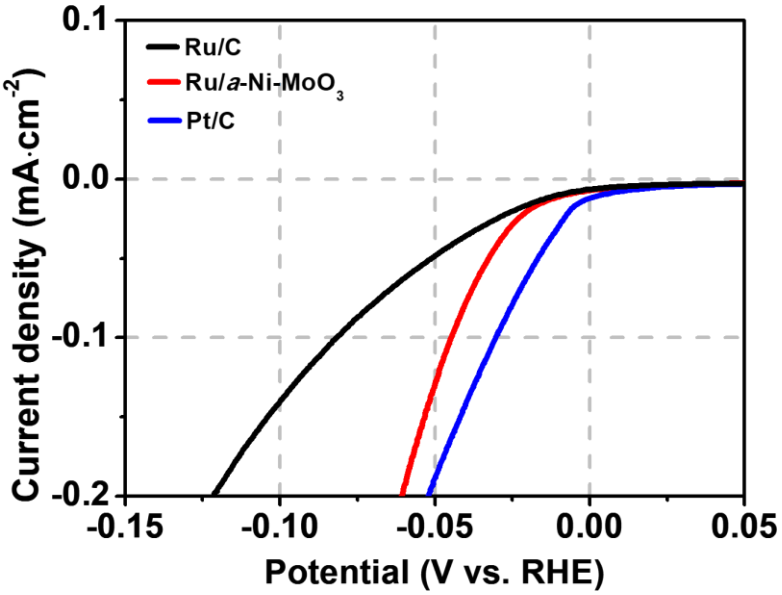

Figure S17. ECSA-normalized polarization curves of Ru/C, Ru/*a*-Ni-MoO_3, and Pt/C in 1 M KOH; scan rate: 5 mV/s.

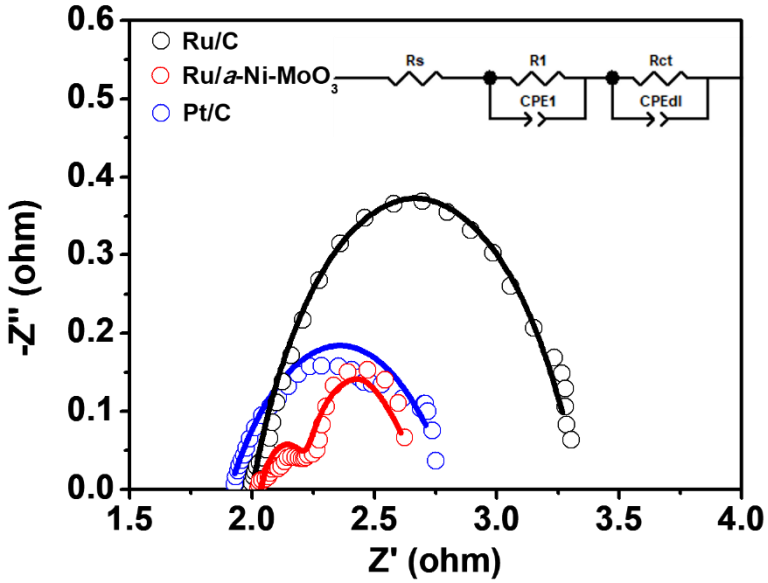

Figure S18. EIS spectra of Ru/C, Ru/*a*-Ni-MoO_3, and Pt/C under an overpotential of -75 mV in 1 M KOH. Inset shows the equivalent circuit model.

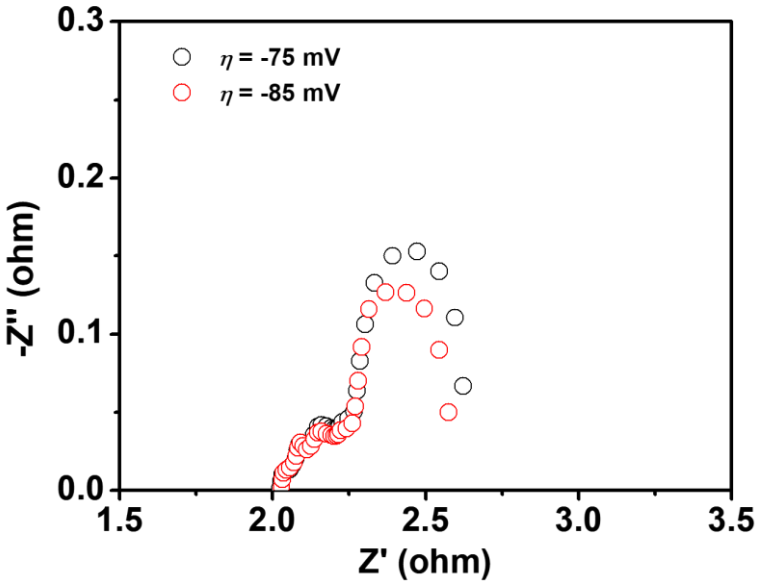

Figure S19. EIS spectra of Ru/*a*-Ni-MoO_3 at overpotentials of -75 and -85 mV in 1 M KOH.

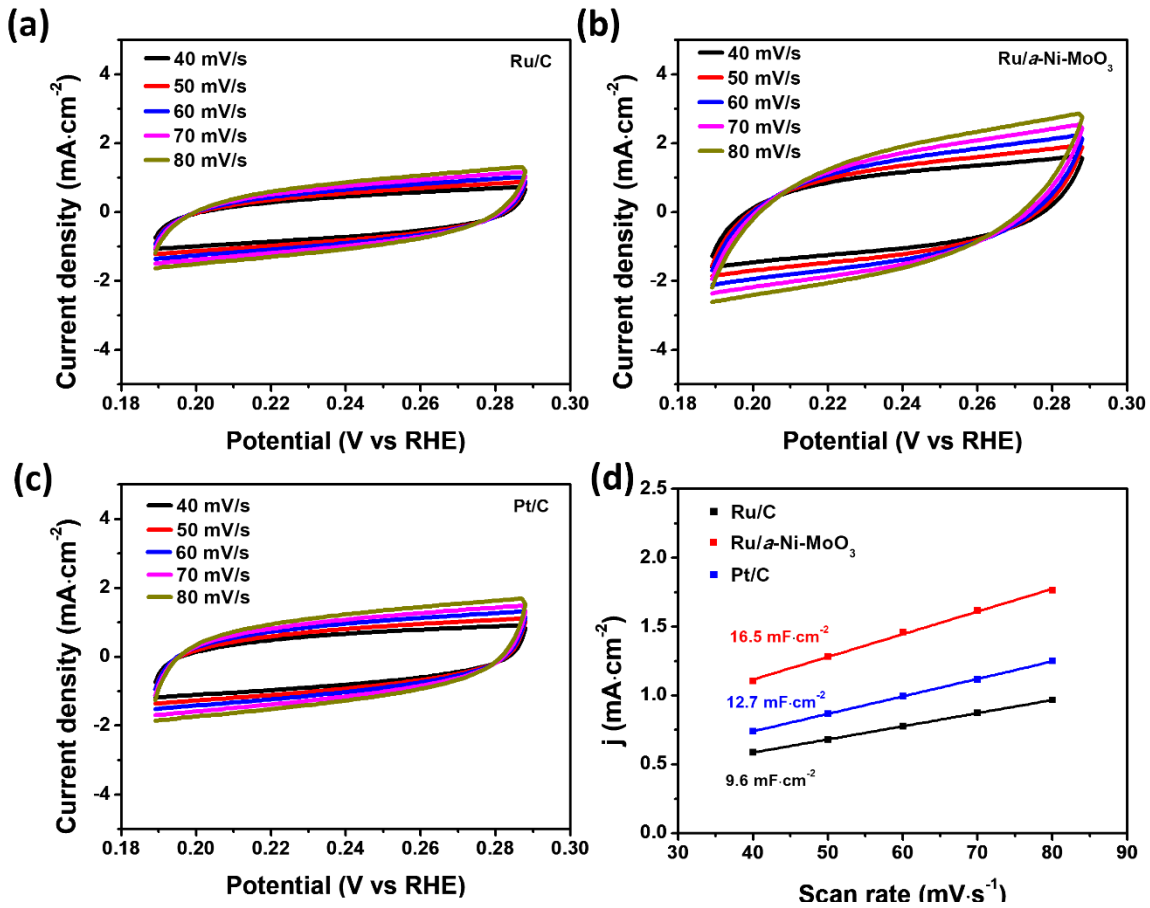

Figure S20. CV curves of (a) Ru/C, (b) Ru/*a*-Ni-MoO_3, and (c) Pt/C in the non-Faradaic regions in 1 M PBS; (d) plots of Δj/2 (the mean value of absolute current density value at the middle point of positive and negative scans in the CV curve) versus scan rate.

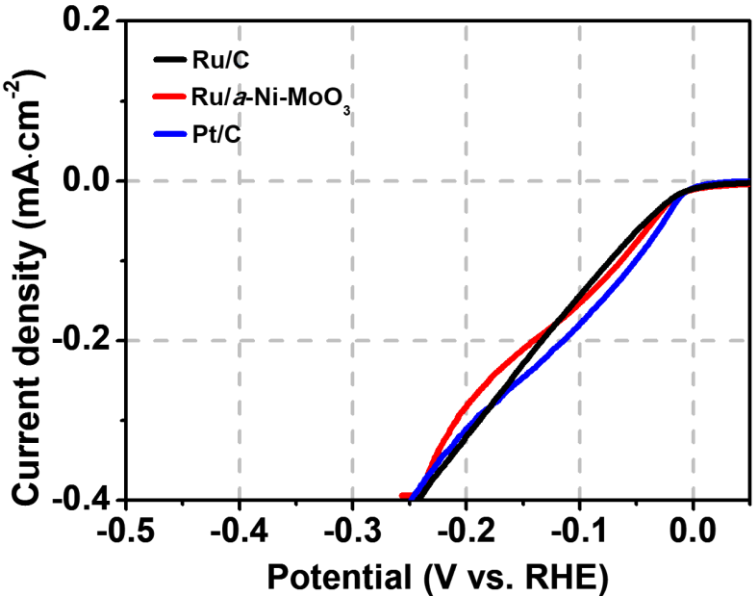

Figure S21. ECSA-normalized polarization curves of Ru/C, Ru/*a*-Ni-MoO_3, and Pt/C in 1 M PBS; scan rate: 5 mV/s.

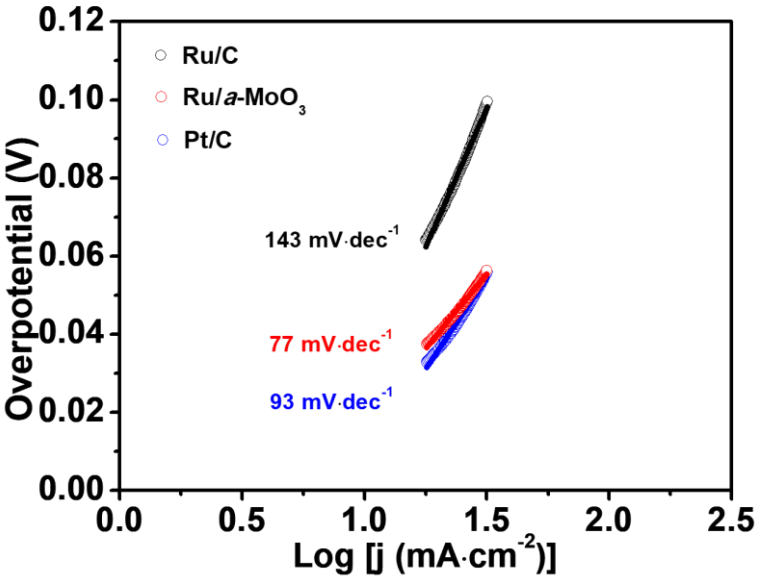

Figure S22. Tafel plots of Ru/C, Ru/*a*-Ni-MoO_3, and Pt/C at large overpotentials in 1 M PBS.

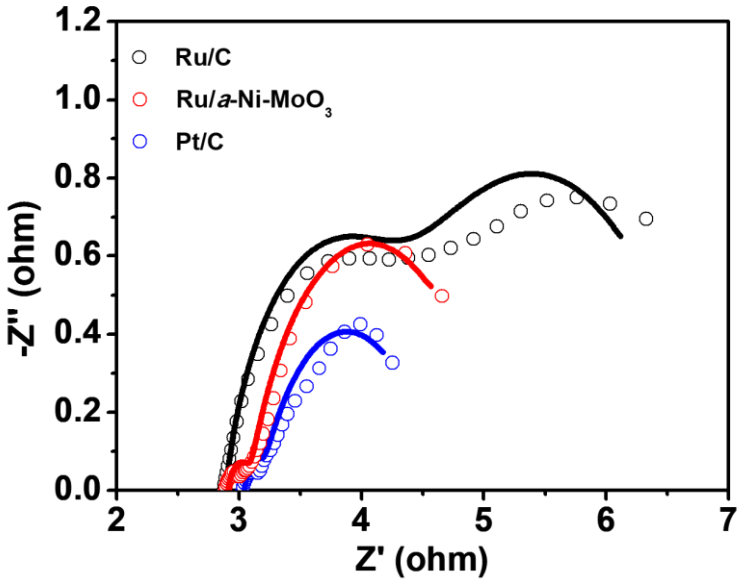

Figure S23. EIS spectra of Ru/C, Ru/*a*-Ni-MoO_3, and Pt/C under an overpotential of -57 mV in 1 M PBS.

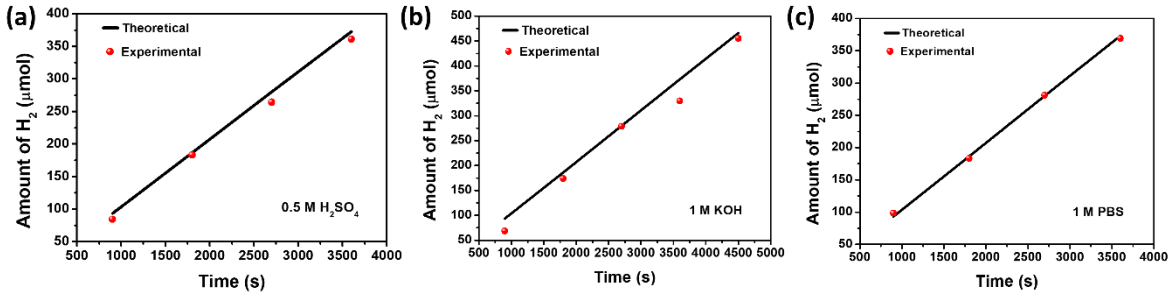

Figure S24. Experimentally measured H_2 production amounts on Ru/*a*-Ni-MoO_3 and the theoretically calculated values with electrolysis time in (a) 0.5 M H_2SO_4, (b) 1 M KOH, and (c) 1 M PBS; applied cathodic current density: 20 mA/cm^2.

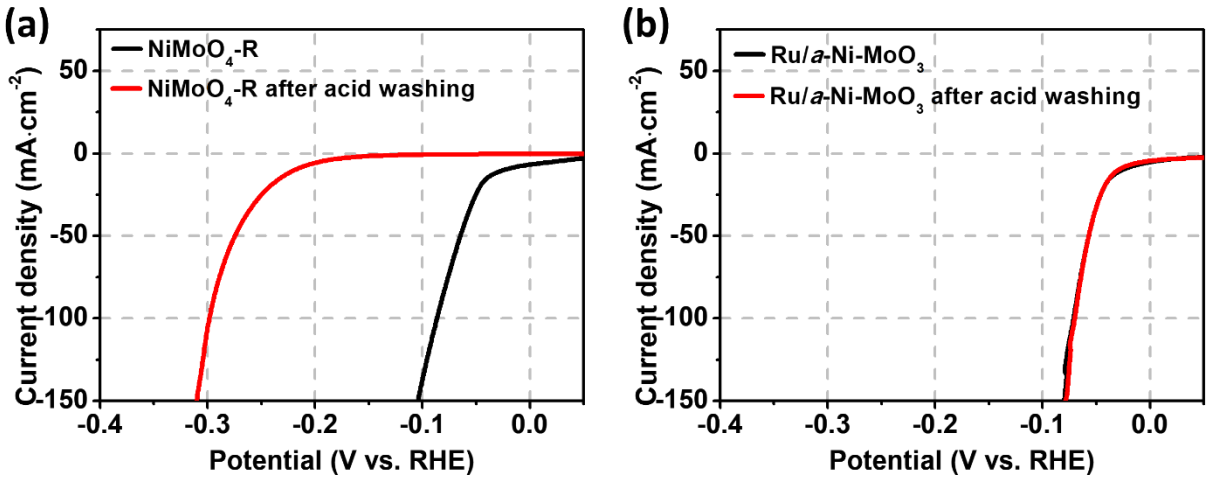

Figure S25. Comparison of polarization curves in 0.5 M H_2SO_4 before and after acid washing of (a) $NiMoO_4$-R and (b) Ru/*a*-Ni-MoO_3. Scan rate: 5 mV/s.

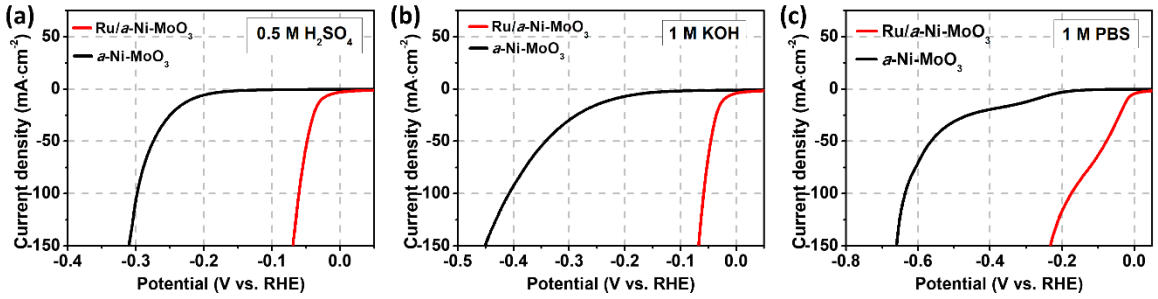

Figure S26. Polarization curves of Ru/*a*-Ni-MoO_3 and *a*-Ni-MoO_3 in (a) 0.5 M H_2SO_4, (b) 1 M KOH, and (c) 1 M PBS. Scan rate: 5 mV/s.

Table S1. ICP-MS measurement results of Ru/a-Ni-MoO_3 on ACC based on an average density of 12 mg/cm^2 for ACC.

	Ni	Mo	Ru
Metal element weight ratio on ACC (%)	0.4	0.96	2.8
Metal element loading on ACC (mg/cm^2)	0.05	0.12	0.35
Metal element relative atomic ratio (%)	15.30	22.47	62.22

Table S2. Quantitative XPS analyses of Ru chemical states in Ru/C and Ru/a-Ni-MoO_3.

		Ru/C	Ru/*α*-Ni-MoO_3
Ru(IV) 3p 3/2	Binding energy (eV)	462.44	462.97
	Percentage of peak (%)	76.05	76.05
Ru(IV) 3p 3/2 sat.	Binding energy (eV)	465.34	465.87
	Percentage of peak (%)	23.95	23.95
Ru(IV) 3d5/2	Binding energy (eV)	280.76	281.2
	Percentage of peak (%)	28.41	27.47
Ru(IV) 3d 3/2	Binding energy (eV)	284.93	285.37
	Percentage of peak (%)	19.03	18.41
Ru(IV) 3d 5/2 sat.	Binding energy (eV)	282.66	283.1
	Percentage of peak (%)	13.41	10.56
Ru(IV) 3d 3/2 sat.	Binding energy (eV)	286.83	287.27
	Percentage of peak (%)	8.98	7.08
C	Binding energy (eV)	284.45	284.51
	Percentage of peak (%)	30.17	36.48

Table S3. Quantitative XPS analyses of Ni and Mo chemical states in $NiMoO_4$-R and Ru/*a*-Ni-MoO_3.

		$NiMoO_4$-R	Ru/*a*-Ni-MoO_3
Ni (II)	Binding energy (eV)	856.13	855.67
	Percentage of peak (%)	76.94	100
Ni (0)	Binding energy (eV)	852.75	N/A
	Percentage of peak (%)	23.06	0
Mo(VI) 3d 3/2	Binding energy (eV)	235.59	235.4
	Percentage of peak (%)	14.15	21.12
Mo(VI) 3d 5/2	Binding energy (eV)	232.49	232.3
	Percentage of peak (%)	21.23	31.69
Mo(VI)	Percentage of peak (%)	35.38	52.81
Mo(V) 3d 3/2	Binding energy (eV)	233.84	234.39
	Percentage of peak (%)	11.46	13.09
Mo(V) 3d 5/2	Binding energy (eV)	230.74	231.29
	Percentage of peak (%)	17.18	19.64
Mo(V)	Percentage of peak (%)	28.64	32.73
Mo(IV) 3d 3/2	Binding energy (eV)	232.78	233
	Percentage of peak (%)	14.39	5.78
Mo(IV) 3d 5/2	Binding energy (eV)	229.68	229.9
	Percentage of peak (%)	21.59	8.67
Mo(IV)	Percentage of peak (%)	35.98	14.45

Table S4. Applied potentials and recorded current densities in chronoamperometry stability test of Ru/C, Ru/*a*-Ni-MoO_3, and Pt/C in different media.

		Applied potential (V vs RHE)	Starting current density (mA/cm²)	Current density after 14 h (mA/cm²)	Current retention after 14 h (%)
0.5 M H_2SO_4	Ru/C	-0.202	-55.21	-33.55	60.77
	Ru/*a*-Ni-MoO_3	-0.174	-50.84	-43.49	85.54
	Pt/C	-0.159	-51.15	-35.68	69.76
1 M KOH	Ru/C	-0.159	-53.85	-52.09	96.73
	Ru/*a*-Ni-MoO_3	-0.149	-49.6	-48.3	97.38
	Pt/C	-0.129	-51.46	-39.51	76.78
1 M PBS	Ru/C	-0.087	-10.96	-4.633	42.27
	Ru/*a*-Ni-MoO_3	-0.07	-10.83	-3.428	31.65
	Pt/C	-0.026	-10.98	-10.95	99.73

Table S5. Equivalent circuit parameters obtained from EIS spectra fitting of Ru/C, Ru/*a*-Ni-MoO_3, and Pt/C in electrolytes with different pH values. In the models, R_s is the solution resistance, R_{ct} and CPE_{dl} are the resistance and constant phase element (CPE) associated with charge transfer, while R_1 and CPE_1 are the corresponding components for the porosity of the electrode. CPE is defined by two values, CPE-T (CPE constant) and CPE-P (CPE exponent).

		R_s	R_{ct}	CPE_{dl}-T	CPE_{dl}-P	R_1	CPE_1-T	CPE_1-P
0.5 M H_2SO_4	Ru/C	2.06	2.751	0.019508	0.73804	0.010844	0.000159	1.524
	Ru/*a*-Ni-MoO_3	1.918	0.64428	4.417	0.90331	0.31981	0.098203	0.70896
	Pt/C	1.982	0.67561	0.6763	0.71688	0.060196	0.008804	1.028
1 M KOH	Ru/C	2.002	1.329	0.056254	0.68516			
	Ru/*a*-Ni-MoO_3	2.037	0.19415	0.16025	0.68019	0.41285	5.047	0.83761
	Pt/C	1.909	0.89953	0.15007	0.50875			
1 M PBS	Ru/C	2.891	2.518	0.25564	0.69134	1.38	0.017655	0.7993
	Ru/*a*-Ni-MoO_3	2.912	1.969	1.772	0.73785	0.17285	0.091408	0.78103
	Pt/C	3.047	1.416	0.48969	0.66668	0.12723	0.018787	0.91748

Table S6. Measured H_2 production amounts, theoretically calculated values, and Faraday efficiencies of Ru/*a*-Ni-MoO_3 in different media; applied cathodic current density: 20 mA/cm^2.

0.5 M H_2SO_4	**Time (s)**	**900**	**1800**	**2700**	**3600**	
	Measured amount (μmol)	84.3	183.3	264.4	361.2	
	Theoretical amount (μmol)	93.3	186.5	279.8	373.1	
	Faraday efficiency (%)	90.4	98.3	94.5	96.8	
1 M KOH	**Time (s)**	**900**	**1800**	**2700**	**3600**	**4500**
	Measured amount (μmol)	68.5	173.5	278.6	329.4	455.3
	Theoretical amount (μmol)	93.3	186.5	279.8	373.1	466.3
	Faraday efficiency (%)	73.4	93.0	99.6	88.3	97.6
1 M PBS	**Time (s)**	**900**	**1800**	**2700**	**3600**	
	Measured amount (μmol)	98.2	183.2	281.0	368.9	
	Theoretical amount (μmol)	93.3	186.5	279.8	373.1	
	Faraday efficiency (%)	105.3	98.2	100.4	98.9	